Nanotechnology

PURPOSE-LED PUBLISHING™

PAPER • OPEN ACCESS

Enhanced LWIR response of InP/InAsP quantum discs-in-nanowire array photodetectors by photogating and ultra-thin ITO contacts

To cite this article: Hossein Jeddi *et al* 2024 *Nanotechnology* **35** 215206

View the article online for updates and enhancements.

You may also like

- Antimonide-based high operating temperature infrared photodetectors and focal plane arrays: a review and outlook
Chunyang Jia, Gongrong Deng, Lining Liu et al.

- Metrological analysis of the three-dimensional reconstruction based on close-range photogrammetry and the fusion of long-wave infrared and visible-light images
Bernardo C F de Oliveira, Guilherme C Marcellino, Pablo A da Rosa et al.

- Development of long-wavelength infrared detector and its space-based application requirements
Junku Liu, , Lin Xiao et al.

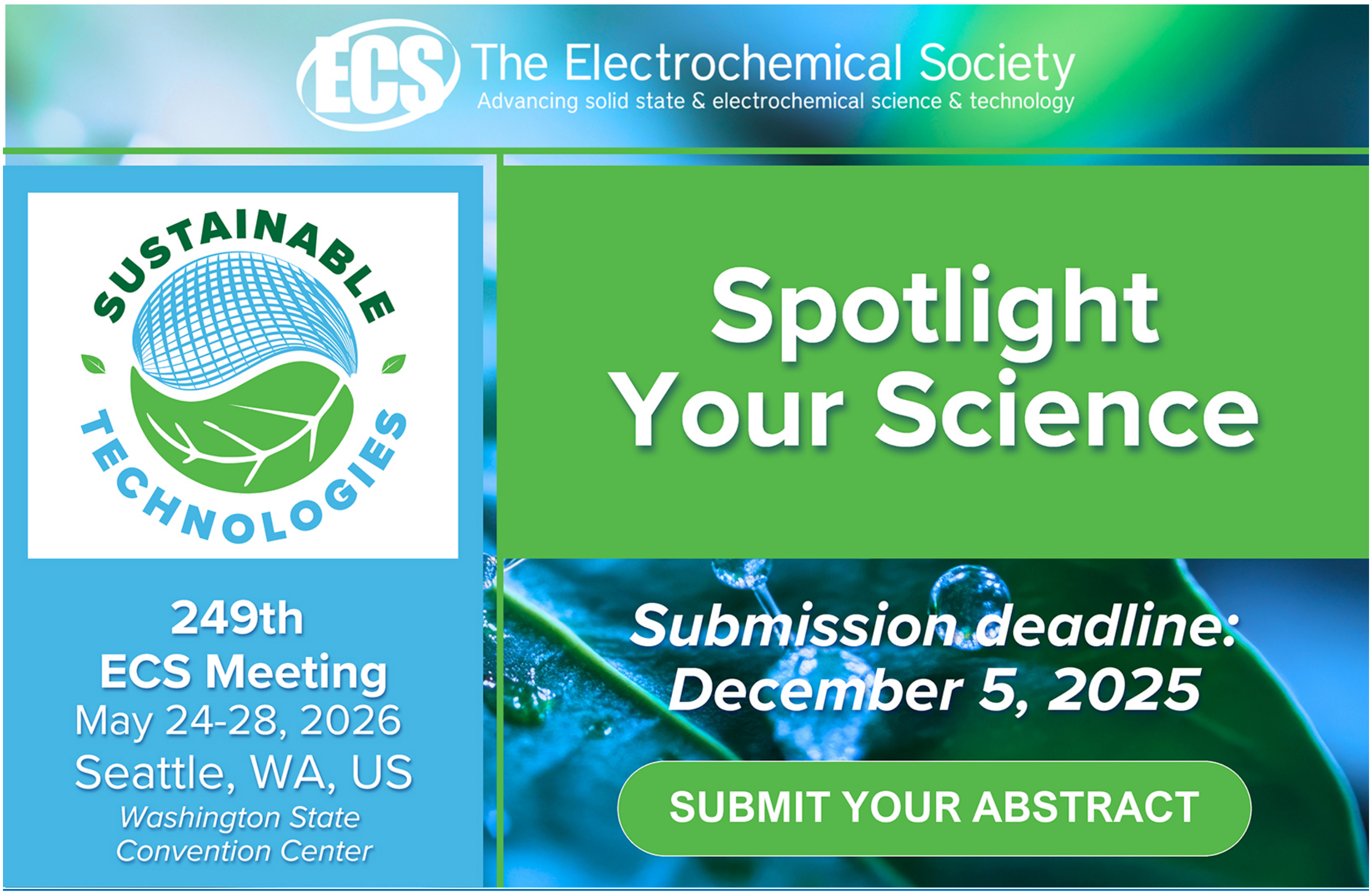

This content was downloaded from IP address 186.244.66.169 on 09/11/2025 at 16:14

OPEN ACCESS
IOP Publishing
Nanotechnology
Nanotechnology **35** (2024) 215206 (7pp)
https://doi.org/10.1088/1361-6528/ad2bd0

Enhanced LWIR response of InP/InAsP quantum discs-in-nanowire array photodetectors by photogating and ultra-thin ITO contacts

Hossein Jeddi[1,2], Kristi Adham[1], Yue Zhao[1], Bernd Witzigmann[3], Friedhard Römer[3], Marie Bermeo[1], Magnus T Borgström[1] and Håkan Pettersson[1,2]

[1] Solid State Physics and NanoLund, Lund University, Box 118, SE-221 00 Lund, Sweden
[2] School of Information Technology, Halmstad University, Box 823, SE-301 18 Halmstad, Sweden
[3] Institute for Optoelectronics, Friedrich-Alexander Universität Erlangen-Nürnberg, Konrad-Zuse Str. 3/5, D-91052 Erlangen, Germany

E-mail: hakan.pettersson@hh.se

Received 16 January 2024, revised 9 February 2024
Accepted for publication 21 February 2024
Published 8 March 2024

Abstract
Here we report on an experimental and theoretical investigation of the long-wavelength infrared (LWIR) photoresponse of photodetectors based on arrays of three million InP nanowires with axially embedded InAsP quantum discs. An ultra-thin top indium tin oxide contact combined with a novel photogating mechanism facilitates an improved LWIR normal incidence sensitivity in contrast to traditional planar quantum well photodetectors. The electronic structure of the quantum discs, including strain and defect-induced photogating effects, and optical transition matrix elements were calculated by an 8-band $\mathbf{k}\cdot\mathbf{p}$ simulation along with solving drift-diffusion equations to unravel the physics behind the generation of narrow linewidth intersubband signals observed from the quantum discs.

Supplementary material for this article is available online

Keywords: infrared photodetectors, nanowires, quantum discs-in-nanowires, nanowire array photodetectors, long-wavelength infrared (LWIR), ultra-thin ITO contacts, photogating

Photodetectors with the capability of converting ultraviolet, visible and infrared (IR) light into electrical signals are key components in many applications e.g. industrial optoelectronics, communication technology, medicine and healthcare, environmental monitoring, safety, and automotive. The LWIR (8–15 μm range has attracted an increasing attention due to thermal emission signatures from objects and living organisms which facilitate a broad range of imaging and night vision capabilities [1, 2]. During the last decades, different materials and device structures have been suggested for LWIR detectors [3]. Today, the most common planar material structures include HgCdTe (MCT) [4], and quantum structures including InAs/GaSb type-II superlattices [5], quantum wells (QWs) [6] and quantum dots (QDs) [7].

III–V compound semiconductor nanowires (NWs) have attracted a strong research and development interest that stems from their quasi-1D character offering key advantages for optoelectronics, including bottom-up growth of complex direct bandgap heterostructures, strong absorption due to nanophotonic resonances, and a potential compatibility with mainstream silicon platforms [8–10]. Recent progress in NW array growth and device processing has led to the development of both radial [11] and axial [12–14] IR detectors. Previously we

Original content from this work may be used under the terms of the Creative Commons Attribution 4.0 licence. Any further distribution of this work must maintain attribution to the author(s) and the title of the work, journal citation and DOI.

© 2024 The Author(s). Published by IOP Publishing Ltd

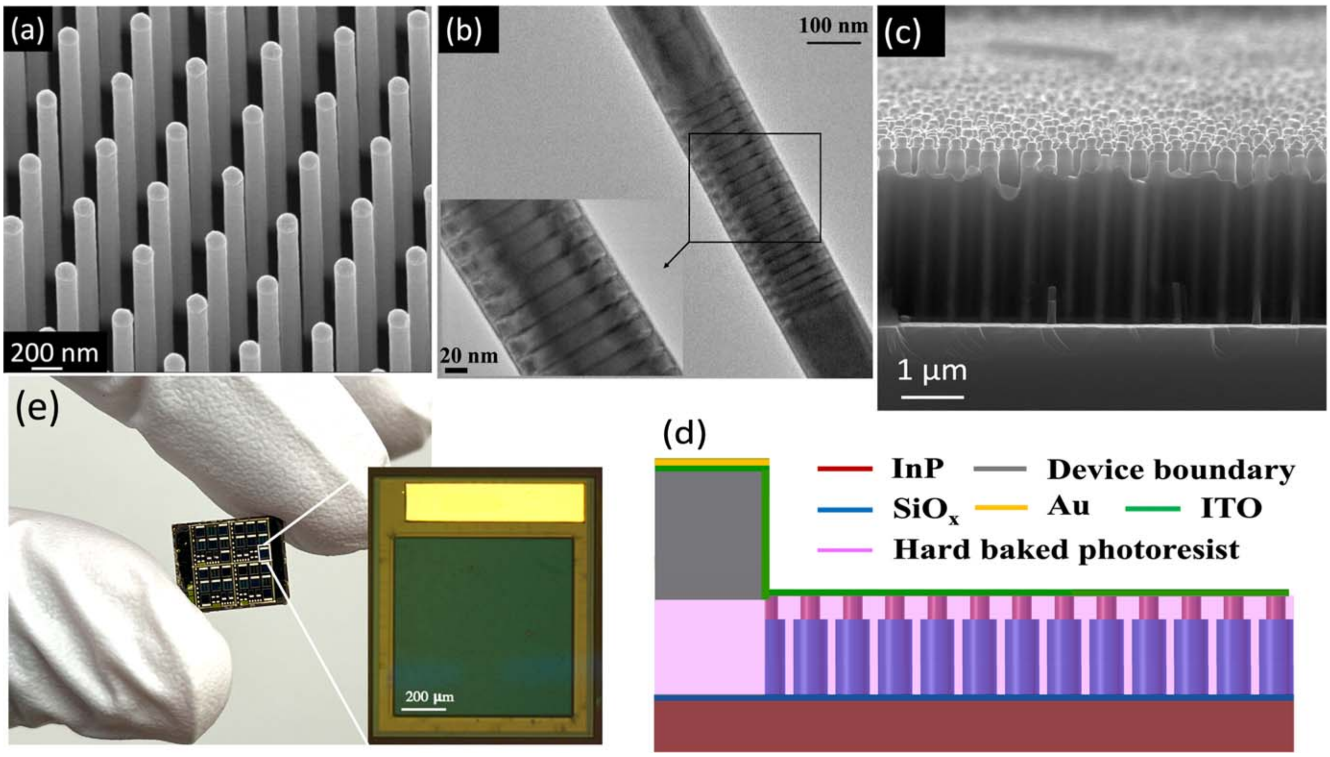

Figure 1. (a) SEM image of the as-grown NWs, (b) TEM image of a single NW with a zoomed-in inset of the QDiscs, (c) cross-sectional SEM image of nanowires inside a device after sputtering of the ultra-thin ITO top contact, (d) cross-sectional schematic of the device, and (e) photograph of a fully processed sample with a zoomed-in inset of one of the largest devices (0.64 mm^2).

reported on the first LWIR intersubband photocurrent (PC) generation (12 μm) in large NW arrays comprising axially embedded InAsP quantum discs (QDiscs) [15]. More recently, single-crystal InSb nanostructures were successfully grown on silicon using rapid melt growth. Residual strain and occasional crystal defects in the nanostructures caused a redshift of the expected mid-wavelength IR (MIR, 3–8 μm) photoresponse onset into the LWIR range (10 μm) [16].

Over the last years, we have reported several studies of two-terminal photoconductors and gate-all-around three-terminal phototransistors based on large arrays of InP NWs with axially embedded InAsP QDiscs for different regions in the visible-to-IR region [14, 15, 17, 18]. Here we report on a detailed theoretical and optical study of the LWIR response in improved two-terminal InP/InAsP NW/QDisc photodetectors using an ultra-thin indium tin oxide (ITO) layer as transparent top contact. The electronic structure of the QDiscs, including strain and defect-induced photogating effects, and optical transition matrix elements were calculated using the 8-band **k·p** method along with solving drift-diffusion equations. The results reveal new intriguing physics behind the observed narrow linewidth of the intersubband signal and the effect of photogating for electrical injection of electrons into the QDiscs.

1. Method

The investigated n$^+$–i–n$^+$ InP NW arrays with 20 InAsP QDiscs embedded in the i-segment of each NW were grown by metalorganic vapor-phase epitaxy (MOVPE) on an n$^+$-InP (111)B substrate patterned with Au nanoparticles (NPs). Trimethylindium (TMIn) and phosphine (PH_3) were used as the precursor for In and P, respectively. Tetraethyltin (TESn) was used as the doping precursor during synthesis of the n-segments, while diethylzinc (DEZn) was used during the growth of the i-segment of InP to compensate residual unintentional n-doping [19]. The detailed growth of the NWs is described elsewhere [14, 18]. Figure 1(a) shows a scanning electron microscopy (SEM) image of the as-grown NWs with a length of 2 μm and a diameter of 135 nm. Each NW comprises 500 nm long bottom n$^+$- and top n$^+$-segments, while the middle 1 μm compensation-doped segment is nominally intrinsic. Single NWs were investigated by transmission electron microscopy (TEM) and energy-dispersive x-ray (EDX) spectroscopy. Figure 1(b) shows a TEM image of a NW tilted to the $[\bar{1}10]$ zone axis, with a zoomed-in inset image of the i-segment with QDiscs. An average composition of 60% As and 40% P ($InAs_{0.6}P_{0.4}$) was extracted from STEM/EDX point-scan profile along the NW taken in the middle of the individual QDiscs.

For the fabrication of the photodetectors the NWs were first isolated with a conformal atomic layer deposition (ALD) of 60 nm SiO_x and 5 nm Al_2O_3. The NWs were then covered by spin coating a layer of photoresist (S1818), followed by reactive ion etching (RIE) until around 300 nm of the NW tips was exposed. Next, the oxide layers and the Au NPs were etched away by stirring the sample slowly in a buffer oxide etchant (BOE 1:10) for 35 s and in an Au etchant (KI/I2 solution) for 25 s, respectively. Since this oxide etching step

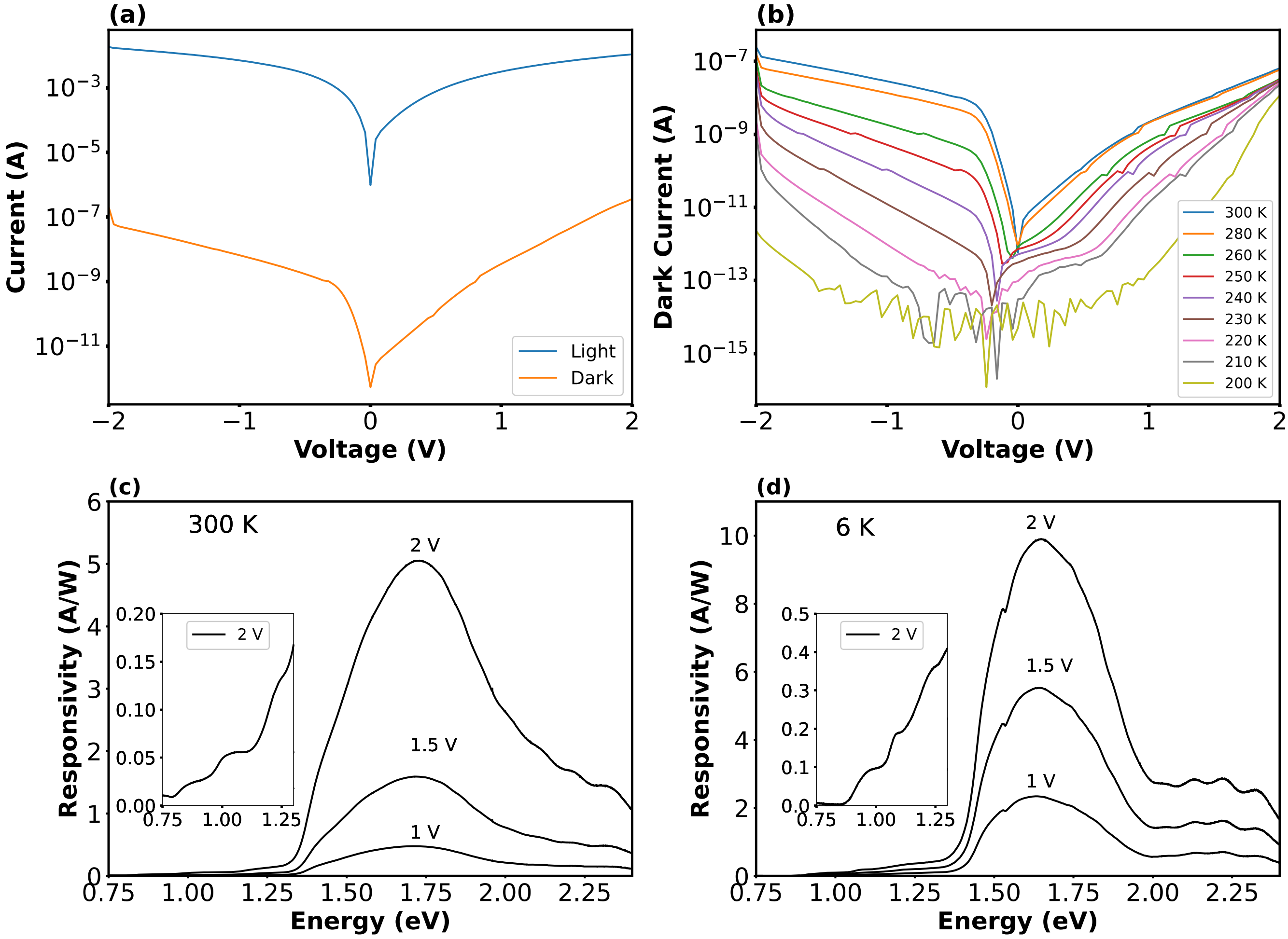

Figure 2. (a) I–V characteristics in dark and under illumination at 300 K. (b) Temperature dependence of the dark current. (c) and (d) Spectrally resolved responsivity at 300 K and 6 K, respectively, at three different biases. The spectral features observed in the inset plots of both (c) and (d) reflect interband transitions in the InAsP QDiscs.

could leave behind a gap between the photoresist and the NWs, potentially leading to a non-uniform top ITO contact formation during the subsequent sputtering, the photoresist layer was washed away by acetone followed by repeated steps of spin coating of new photoresist and RIE. The photoresist was finally hard baked for 15 min at 200 °C. Before sputtering 50 nm ITO (resulting in an ultrathin 10 nm ITO side wall thickness around the tip of the NWs) as the top contact, device areas with various sizes (containing different numbers of NWs) were defined on top of the hard-baked photoresist using ultraviolet lithography (UVL), followed by a second hard-baking step. The native oxide on the NWs was etched for 30 s (H_2SO_4) right before mounting the sample in the sputter. The sputtered ITO layer was etched from non-device areas by stirring the sample slowly in HCl for 2 min, while the device areas were covered by a photoresist layer deposited in an UVL session. The last session of the fabrication process included definition of the bond pad on top of each device using a negative photoresist (Ma-N 490) and UVL, evaporation of 20 nm Ti/400 nm Au and then lift-off in acetone. Figure 1(c) shows a cross-sectional SEM image of the NWs inside a device area. A cross-sectional schematic of a device and an optical image of a fully processed sample are shown in figures 1(d) and (e), respectively. The inset in figure 1(e) shows the largest device (0.64 mm^2) with almost three million NWs connected in parallel. For optoelectronic measurements, the sample was mounted on a DIL holder and individual devices were bonded. During the measurements, the n^+-InP substrate served as the ground contact, while the sputtered ITO top contact was connected to the bias source.

2. Results and discussion

Figure 2(a) shows the I–V characteristics of a 0.64 mm^2 device measured with a Keithley 2636B dual channel source meter in dark and under illumination at 300 K. The total photodetector current, including both dark current and PC, was measured under illumination from the built-in quartz lamp in our evacuated (0.1 mbar) Fourier transform infrared (FTIR) spectrometer (Bruker, Vertex 80V). The small dark current indicates a successful compensation doping using Zn in the i-segment of the NWs. Another reason for the low dark current is acceptor-like trap states located at the interface between the NW and the SiO_x isolation shell [17]. In dark, these traps are filled with electrons which reduces the radial

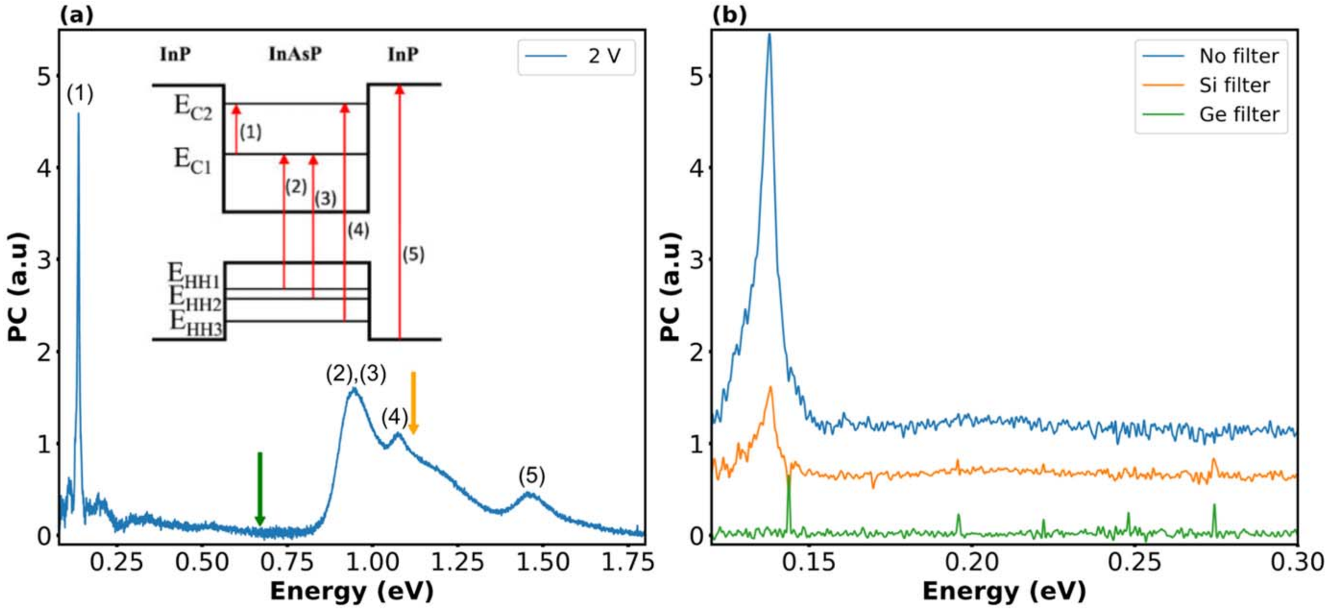

Figure 3. (a) Spectrally resolved normal incidence PC at 6 K recorded in a broad spectral range, revealing both intersubband and interband PC. The interband transitions 2 and 3 cannot be resolved separately here. (b) Zoomed-in spectra showing the intersubband PC, normalized with respect to the photon flux. The band gap energy for the Ge and Si filters used are indicated as green and orange arrows in (a).

width of the electron channel in the NWs by electrostatic depletion. Under illumination, the photogenerated holes are attracted to the interface where they recombine with the negatively charged traps which opens the electron channel. This phenomenon, known as photogating, leads to a very high responsivity investigated in depth in our previous reports [17, 20]. The dark current through the photodetector was furthermore measured as a function of temperature, cooling down from 300 K in a cryostat (Janis SHI-950) integrated with the FTIR spectrometer. The sample was covered by a mm-thick stainless-steel cap to prevent any dark current generation by black body radiation from the surrounding spectrometer. Figure 2(b) shows that the dark current strongly decreases with temperature to the measurement limit of our system (around 10 fA) already at 200 K, which shows the strong combined effect of the Zn doping of the i-segment and photogating. Figure 2(c) shows the spectrally resolved responsivity of the photodetector at room temperature. The responsivity was obtained after a proper conversion of the spectrally resolved PC using NIST-calibrated Si (FDS100-CAL) and Ge (FDG03-CAL) photodiodes, purchased from Thorlabs. The increased responsivity at larger bias can be explained by more efficient photocarrier extraction from both the QDiscs and the NWs. Figure 2(d) shows the spectrally resolved responsivity at 6 K. The spectral features observed below the bandgap of InP in the inset plots of both figures 2(c) and (d) are attributed to interband transitions in the InAsP QDiscs, in excellent agreement with the simulations discussed below (figure 6).

At low temperature, the spectrally resolved PC was also measured using the built-in globar light source in our spectrometer, offering a much higher photon flux in the LWIR range compared to the quartz lamp. A sharp peak at around 135 meV (9.2 μm) is noticeable in figure 3(a). This sharp PC signal reflects an intersubband transition between the ground state and the first excited state in the conduction band of the QDiscs. Furthermore, the interband PC generation in the QDiscs discussed above is also visible in figure 3(a). It should be noted that the PC shown in figure 3(a) is not normalized with respect to photon flux. Evidently, the shape and magnitude of this PC response is different from that in figure 2(d). The reasons for this are two fold: firstly, the spectral distribution of the photon flux from the globar light source is quite different from that of the quartz lamp, and secondly, the beam splitter in the FTIR was changed from CaF_2 to KBr when switching to the globar light source to avoid LWIR absorption by the beam splitter. The blue trace in figure 3(b) shows a zoomed-in part of the spectrum in figure 3(a), focusing on the MWIR-LWIR range, now properly normalized to the photon flux, measured with a built-in pyroelectric deuterated L-alanine doped triglycene sulphate (DLaTGS) detector. Figure 3(b) also shows similar spectra subsequently collected using a Ge filter (green trace) and a Si filter (orange trace), respectively, placed in front of the sample. The Ge filter blocks all interband excitations in QDiscs and NWs, as evident from figure S1. For clarity, a green arrow indicates the bandgap of Ge in figure 3(a). Interestingly, the blocked interband excitation results in a completely lost intersubband PC signal. Replacing the Ge filter with a Si filter (bandgap indicated by the orange arrow in figure 3(a)) blocks all higher energy interband excitations in the QDiscs, and thus all excitations in InP, resulting in a reduced intersubband signal. The Ge and Si filter has around 55% and 30% transmission at 9 μm, respectively, by which the intersubband signal is expected to be reduced by only a factor of two-to-three. We conclude that an interband pumping process is crucial for observing an intersubband signal. This can be explained by the above-mentioned photogating effect. Under

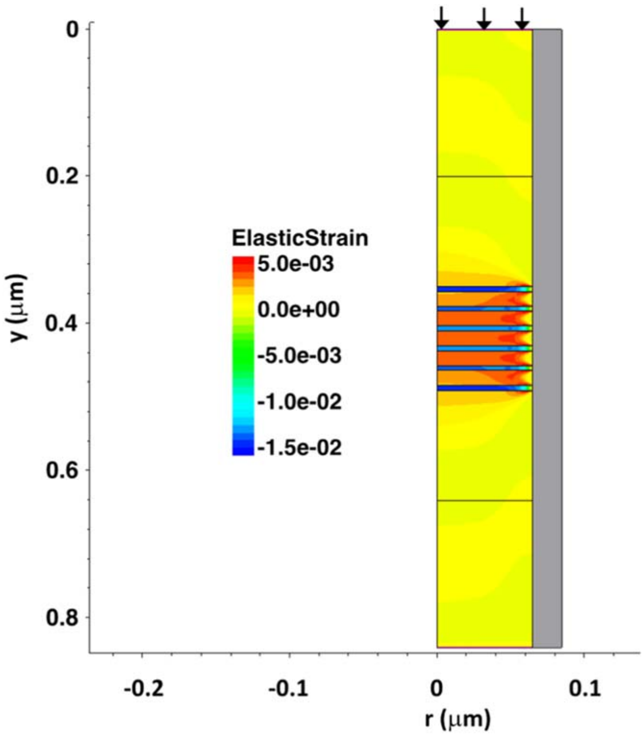

Figure 4. Calculated radial trace of the strain tensor for the developed NW model; the QDiscs show compressive strain, and the barriers tensile strain. The arrows at the top indicate the radial positions where subband calculations have been performed for the QDiscs. The grey-colored stripe to the right indicates the SiO_x shell around the NW.

interband illumination the conduction channel in the NWs gets wider and more electrons are injected into the i-segment of the NWs and captured into the ground state of the QDiscs. Moreover, optical interband transitions involving discrete electron and hole states in the QDiscs can directly feed the electron ground state of the QDiscs.

In order to analyze the electronic structure of the QDiscs, and related optical transitions observed in figure 3, an 8-band **k**·**p** simulation coupled to a drift-diffusion transport solver at $T = 300$ K was applied to a rotationally symmetric 2D NW/QDisc structure with only 6 QDiscs shown in figure 4. Simulating a larger number of QDiscs showed unstable numerical convergence of the Schrödinger–Poisson system in the strongly depleted intrinsic region. A 3D simulation at low temperature of the full structure is beyond the computational capabilities. The reduced physical model was scaled in a consistent way to ensure that all extracted physical parameters were accurate and directly comparable to the experimental data. Figure 4 shows the radial trace of the calculated strain tensor for the developed model. The QDiscs are under compressive strain, which varies in the radial direction. In contrast to a biaxial approximation for an infinite layered system, there is strain release towards the NW surface. Moreover, the InP barriers between the QDiscs exhibit tensile strain (approx. 0.5%). Both effects lead to a reduction of total strain energy, and therefore significantly improved crystal quality in the nanostructure.

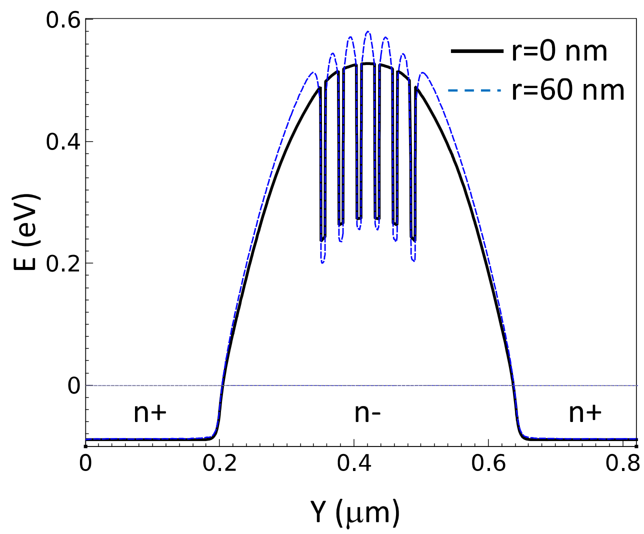

Figure 5. Conduction band profile at 0 V bias along the NW center ($r = 0$ nm, solid black line) and close to the NW surface ($r = 60$ nm, dashed blue line).

The **k**·**p** method is applied to each of the six individual QDiscs along three vertical cuts through the structure at different radii (r = 1 nm, 30 nm, and 60 nm), indicated by the three arrows at the top of the schematic of the NW in figure 4. Thus, a total of 18 **k**·**p** problems are solved for the complete system. Figure 5 displays the conduction band profile along a NW at V= 0 V in the NW center and close to the NW surface, respectively. Due to the strain-induced band edge shifts, and the electron traps at the NW/oxide interface (discussed briefly above), the conduction band is warped, leading to a deeper radial confinement potential at the NW surface.

The subband dispersion from the **k**·**p** calculation gives the energy levels shown in figure 6. Also, the polarization resolved matrix elements for interband and intersubband transitions have been extracted. For this calculation the voltage at the contacts has been chosen $V = 0.8$ V, which introduces an electric field across the QDiscs in the reduced simulation structure similar to that at $V = 2.0$ V applied in the experiments. Matrix elements for interband transitions with non-zero entries are the following: for in-plane polarization neglecting excitonic shifts, E_{C1}–E_{HH1} (0.90 eV), E_{C1}–E_{HH2} (0.95 eV), and E_{C2}–E_{HH3} (1.10 eV). In an ideal QW, the transitions involving states with different parity would not be allowed.

Due to the strong band-band coupling (strain), however, these transitions show a finite matrix element. These calculated transition energies are in good agreement with the experimental data shown in figures 2(c) and 3(a). For direct comparison to the low temperature data in figure 2(d), a thermal Varshni-type blue-shift of 120 meV needs to be added to these simulated values [21]. The intersubband matrix elements show non-zero entries only for the out-of plane polarization with the transition E_{C2}–E_{C1} at an energy of 130 meV in good agreement with the experimental results in figure 3. The simulated intersubband transition needs to be red shifted for direct comparison to the low temperature data;

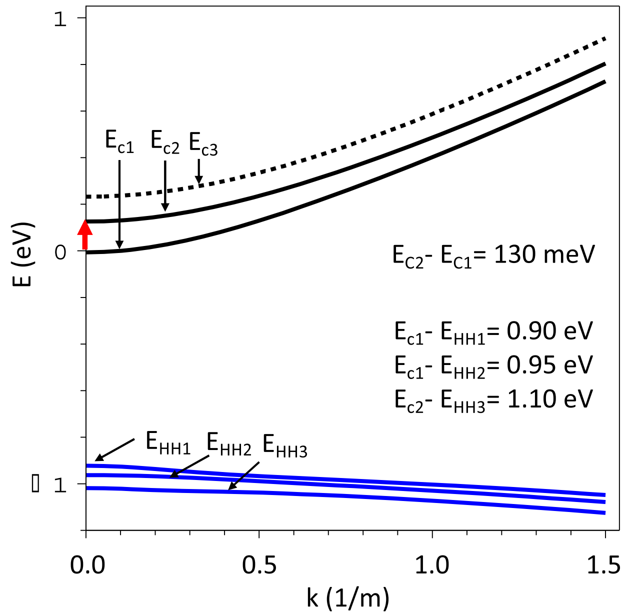

Figure 6. Band dispersion relations from an 8-band **k**·**p**-simulation of a single QDisc, showing the relevant interband and intersubband transitions also discussed in figures 2 and 3. The intersubband transition from E_{C1} to E_{C2} is shown with a red arrow at $k = 0$.

a thermal red shift for intersubband transitions of 8 meV has been reported for cooling down from 300 to 4 K [22]. Overall, the calculated optical interband and intersubband transition energies are in very good agreement with the experimental data presented in figures 2 and 3. Interestingly, the selection rules require out-of plane polarization in contrast to the experimental in-plane conditions (figure 3). Similar results were reported by us previously in our seminal demonstration of the first intersubband LWIR PC response in NW/QDisc structures. We concluded there that the device structure in fact displays photonic crystal effects which effectively scatters the IR radiation leading to a significant longitudinal component along the NWs. A related intriguing observation is that the intersubband PC decreases when the sample is rotated from normal incidence conditions, again in contrast to the above-mentioned selection rules for quantum wells. We attribute this to a decreasing electron population in the ground state E_{C1} of the QDiscs under tilted conditions, resulting primarily from a reduced photogating effect but also to a weaker direct optical interband pumping of the ground state as discussed above. An optical interband pumping is indeed needed to load electrons into the ground state of the QDiscs in order to induce intersubband transitions. Simulations show that in dark the electron density in the QDiscs at $V = 0.8$ V and $T = 300$ K (which creates a similar bias as 2 V in the experiments) is only about $2 \times 10^{15}\mathrm{cm}^{-3}$, resulting from the depletion due to interface trap charges and low doping density in the nominal i-segment of the NW comprising the QDiscs. Under interband excitation, this concentration increases by two orders of magnitude. Interestingly, the variation of the intersubband transition energy in our simulations due to inhomogeneities in the structure (local electric field, strain, and charge density) is within 5 meV, which in part explains the narrow FWHM of about 5 meV in the experiments (in fact similar to typical high-quality planar quantum well IR photodetectors [23]). Interestingly, the electron energy level E_{C3} in figure 6 only occurs in the vicinity of the NW surface, where the QDisc potential is warped resulting in a deeper confinement potential (see figure 5) and an additional bound electron state. The improved signal-to-noise ratio (SNR) of the sharp intersubband peak (compared to our previously published results [15]) is due to the improved processing, especially the development of an ultra-thin ITO top contact. It is well known that ITO has a very strong absorption in the LWIR region, wherefore it is typically not implemented as transparent contacts in this spectral range. Figure S2 shows the transmission through layers of ITO with different thickness sputtered onto an undoped silicon substrate. Clearly, 150 nm of ITO, which was used in our previous processing [15], exhibits a drastic absorption in the LWIR range. In the current processing scheme, we have used 50 nm of ITO that significantly improves the transmission by almost three times around 9 μm. From figure 1(c) it is evident that the side wall deposition of ITO around the tip of the NWs is even thinner and amounts to only 10 nm.

Another crucial factor for the performance of the detector is the sheet resistance of the thin ITO layer. We used the familiar four-point probe technique to measure the sheet resistance of sputtered ITO layers with different thickness. The well-known textbook formula $R_s = 4.53236\ \frac{\Delta V}{I}$ was used to calculate the sheet resistance, where I is the applied current to the outer two probes and ΔV is the measured voltage between the two inner probes. Figure S3 shows the sheet resistance of the ITO layer versus thickness. The sheet resistance of the ITO layer increases from 55 $\Omega\mathrm{sq}^{-1}$ for 150 nm to 220 $\Omega\mathrm{sq}^{-1}$ and 2500 $\Omega\mathrm{sq}^{-1}$ for 50 nm and 10 nm thickness, respectively. Atomic force microscopy (AFM) was used to investigate the morphology and surface roughness of the ultra-thin ITO layers. As evident from figure S4, no degradation was observed for an ultra-thin 10 nm ITO layer as compared to a 150 nm thick layer.

3. Conclusions

An in-depth theoretical and experimental investigation of InP/InAsP QDiscs-in-NW photodetectors with an ultra-thin ITO top contact is reported. The photodetector shows a photoresponse from the visible to the LWIR region based on optical interband and intersubband transitions in the InP NW segments and axially embedded QDiscs. The measurements show that the ultra-thin ITO layer improves the IR transmission drastically, which results in an enhancement of the PC generated through intersubband transitions around 9 μm between the ground and first excited state of the QDiscs. The observed interband and intersubband transitions in the QDiscs are in very good agreement with the calculated electronic structure of the QDiscs, including strain and defect-induced photogating effects, and optical transition matrix elements using an 8-band k·p simulation along with self-consistent drift-diffusion equations.

Acknowledgments

The authors would like to acknowledge financial support from the Swedish Research Council (project IDs: 2018–04722 and 2018–04640), the European Union's Horizon 2020 Research and Innovation Programme under the Marie Skłodowska-Curie grant agreement no. 945378, NanoLund and Myfab. Further support from the federal state of Hesse, Germany, within the SMolBits project in the LOEWE program is also acknowledged.

Data availability statement

The data cannot be made publicly available upon publication because no suitable repository exists for hosting data in this field of study. The data that support the findings of this study are available upon reasonable request from the authors.

ORCID iDs

Hossein Jeddi https://orcid.org/0000-0002-9939-2395
Kristi Adham https://orcid.org/0000-0002-6681-204X
Yue Zhao https://orcid.org/0000-0002-1694-3236
Bernd Witzigmann https://orcid.org/0000-0001-9705-9516
Friedhard Römer https://orcid.org/0009-0001-5665-0083
Marie Bermeo https://orcid.org/0000-0003-2316-4756
Magnus T Borgström https://orcid.org/0000-0001-8061-0746
Håkan Pettersson https://orcid.org/0000-0001-5027-1456

References

[1] Schneider H and Liu H C 2007 *Quantum Well Infrared Photodetectors* (Springer)
[2] Rogalski A 2003 Quantum well photoconductors in infrared detector technology *J. Appl. Phys.* **93** 4355–91
[3] Guan X, Yu X, Periyanagounder D, Benzigar M R, Huang J K, Lin C H, Kim J, Singh S, Hu L and Liu G 2021 Recent progress in short-to long-wave infrared photodetection using 2D materials and heterostructures *Adv. Opt. Mater.* **9** 2001708
[4] Wang Y *et al* 2022 Fast uncooled mid-wavelength infrared photodetectors with heterostructures of van der Waals on epitaxial HgCdTe *Adv. Mater.* **34** 2107772
[5] Ting D Z, Soibel A, Höglund L, Nguyen J, Hill C J, Khoshakhlagh A and Gunapala S D 2011 Type-II superlattice infrared detectors *Semiconductors and Semimetals* (Elsevier) vol 84, pp 1–57
[6] Yang H, Zheng Y, Tang Z, Li N, Zhou X, Chen P and Wang J 2020 MBE growth of high performance very long wavelength InGaAs/GaAs quantum well infrared photodetectors *J. Phys.* D **53** 135110
[7] Ren A, Yuan L, Xu H, Wu J and Wang Z 2019 Recent progress of III–V quantum dot infrared photodetectors on silicon *J. Mater. Chem.* C **7** 14441–53
[8] Hrachowina L, Chen Y, Barrigón E, Wallenberg R and Borgström M T 2022 Realization of axially defined GaInP/InP/InAsP triple-junction photovoltaic nanowires for high-performance solar cells *Mater. Today Energy* **27** 101050
[9] Adham K, Zhao Y, Hrachowina L, Alcer D, Wallenberg R and Borgström M T 2023 Growth of branched nanowires via solution-based Au seed particle deposition *Mater. Res. Express* **10** 085003
[10] Mauthe S, Baumgartner Y, Sousa M, Ding Q, Rossell M D, Schenk A, Czornomaz L and Moselund K E 2020 High-speed III–V nanowire photodetector monolithically integrated on Si *Nat. Commun.* **11** 4565
[11] Wang X, Pan D, Han Y, Sun M, Zhao J and Chen Q 2019 Vis–IR wide-spectrum photodetector at room temperature based on p–n junction-type $GaAs_{1-x}Sb_x$/InAs core–shell nanowire *ACS Appl. Mater. Interfaces* **11** 38973–81
[12] Xing Z, Akter A, Kum H S, Baek Y, Ra Y-H, Yoo G, Lee K, Mi Z and Heo J 2022 Mid-infrared photon sensing using InGaN/GaN nanodisks via intersubband absorption *Sci. Rep.* **12** 4301
[13] Lahnemann J, Ajay A, Den Hertog M I and Monroy E 2017 Near-infrared intersubband photodetection in GaN/AlN nanowires *Nano Lett.* **17** 6954–60
[14] Karimi M *et al* 2017 Room-temperature InP/InAsP quantum discs-in-nanowire infrared photodetectors *Nano Lett.* **17** 3356–62
[15] Karimi M *et al* 2018 Intersubband quantum disc-in-nanowire photodetectors with normal-incidence response in the long-wavelength infrared *Nano Lett.* **18** 365–72
[16] Menon H, Jeddi H, Morgan N P, I Morral A F, Pettersson H and Borg M 2023 Monolithic InSb nanostructure photodetectors on Si using rapid melt growth *Nanoscale Adv.* **5** 1152–62
[17] Jeddi H, Karimi M, Witzigmann B, Zeng X, Hrachowina L, Borgström M T and Pettersson H 2021 Gain and bandwidth of InP nanowire array photodetectors with embedded photogated InAsP quantum discs *Nanoscale* **13** 6227–33
[18] Jeddi H, Witzigmann B, Adham K, Hrachowina L, Borgström M T and Pettersson H 2023 Spectrally tunable broadband gate-all-around InAsP/InP quantum discs-in-nanowire array phototransistors with a high gain-bandwidth product *ACS Photon.* **10** 1748–55
[19] Otnes G, Barrigón E, Sundvall C, Svensson K E, Heurlin M, Siefer G, Samuelson L, Åberg I and Borgström M T 2018 Understanding InP nanowire array solar cell performance by nanoprobe-enabled single nanowire measurements *Nano Lett.* **18** 3038–46
[20] Karimi M, Zeng X, Witzigmann B, Samuelson L, Borgstrom M T and Pettersson H 2019 High responsivity of InP/InAsP nanowire array broadband photodetectors enhanced by optical gating *Nano Lett.* **19** 8424–30
[21] Lee C-Y, Wu M-C, Shiao H-P and Ho W-J 2000 Temperature dependence of photoluminescence from InAsP/InP strained quantum well structures grown by metalorganic chemical vapor deposition *J. Cryst. Growth* **208** 137–44
[22] Larrabee D, Khodaparast G, Kono J, Ueda K, Nakajima Y, Nakai M, Sasa S, Inoue M, Kolokolov K and Li J 2003 Temperature dependence of intersubband transitions in InAs/AlSb quantum wells *Appl. Phys. Lett.* **83** 3936–8
[23] Maier T, Schneider H, Liu H, Walther M and Koidl P 2005 Two-photon QWIPs for quadratic detection of weak mid-infrared laser pulses *Infrared Phys. Technol.* **47** 182–7